# XLS Deliverable D4.3

## Accelerating structure design and fabrication procedure

W. Wuensch[1)][I], M. Aicheler[III], D. Alesini[II], M. Bellaveglia[II],
M. van den Berg[IV], M. Breukers[IV], F. Cardelli[II], M. Diomede[II],
L. Faillace[VII], A. Gallo[II], M. Jacewicz[VI], X. Janssen[IV],
L. Piersanti[II], G. Di Raddo[II], X. Wu[I]

On behalf of the CompactLight Partnership

Prepared on: 30.03.2021

[I] CERN, Switzerland, [II] INFN-LNF, Italy, [III] Helsinki University, Finland, [IV] VDL ETG,
Netherlands, [V] Sapienza University of Rome, Italy, [VI] Uppsala University, Sweden

---

[1] Corresponding author: walter.wuensch@cern.ch

# **Abstract**

This deliverable report describes the complete radio frequency, thermo-mechanical and manufacturing designs of the X-band accelerating structure of the linac of CompactLight followed by the industrialization strategy for it full scale production. The work was carried out in work package 4. The CompactLight linac consists of approximately one hundred 0.9 m long accelerating structures which are important performance and cost drivers for the facility as a whole. The structures operate in both a high-gradient, 65 MV/m and 100 Hz, mode and a high-repetition rate, 30 MV/m and 1 kHz, mode so have demanding gradient and average power requirements. The structure parameters are optimized for both radio frequency and beam dynamics performance and have higher order transverse mode suppression for stable two-bunch operation. The cooling circuit has been designed to accommodate the high average power of the high-repetition rate mode and optimized for minimum difference between operating modes. The mechanical design of the structures has also been analyzed and optimized for industrial production. The design considerations along with the final designs and parameters are presented.

# Contents

# 1 Introduction

This report describes the Radio Frequency (RF), thermo-mechanical and manufacturing designs of the X-band travelling-wave accelerating structure of the linac of CompactLight along with the industrialization strategy for it full scale production. The work was carried out in work package WP4. The CompactLight linac consists of approximately one hundred 0.9 m long travelling-wave accelerating structures. These accelerating structures have a strong impact on the performance and cost of the CompactLight facility as a whole. For example the accelerating gradient directly influences the length of the linac, thus strongly influences the size and cost of the facility. The accelerating structures strongly interact with the electron beam through longitudinal and transverse wakefields, giving a strong dependence on their design of the quality of photon production. Consequently the accelerating structures have been designed to a great level of detail. A full design of the structures has been carried out, including RF, beam dynamics, thermo-mechanical, manufacturing and industrialization considerations. The design options and choices along with the final designs and parameters are presented in this report.

The structures must also be designed to enable special operating conditions that give CompactLight unique experimental capabilities; multiple gradient and repetition rate combinations and two-bunch operation. The extreme gradient – repetition rate combinations are a high-gradient 65 MV/m at 100 Hz mode and a high-repetition rate 30 MV/m at 1 kHz mode. The structure parameters are optimized for both radio frequency and beam dynamics performance and have higher order transverse mode suppression for stable two-bunch operation. The cooling circuit has been designed to accommodate the high average power of the high-repetition rate mode and optimized for minimum difference between operating modes.

The CompactLight linac is composed of X-band modules, described in detail in the CompactLight deliverable D4.2, which each contain four Travelling Wave Accelerating Structures (TWASs) fed by a 50 MW klystron and pulse compressor system. By using pulse compression, one klystron can feed several structures through a waveguide network. Thus, the X-band linac can be composed of a sequence of RF modules, each one with four structures.

There are several important parameters to be determined during optimization, for example the structure length and the profile of the diameter of the irises along the structure length as well as their thickness. These parameters directly influence the total number of structures that are needed for each module and for the linac as a whole, which in turn determines the total required number of klystrons and pulse compressors. One important goal is to maximise the RF efficiency, which has the consequence of minimising the total number of klystrons. The average accelerating gradient and the average iris radius of the structure, which defines the compactness and influences the stability of the machine respectively, are provided by work packages 2 and 6 as input specifications to the electromagnetic design. The study of electromagnetic design is followed by investigating the thermo-mechanical properties, which are presented in sections 2 and 3. Finally in section 4 the route towards an industrialization of the accelerator is described based on a breakdown of the various production processes.

# 2 Electromagnetic Design and Optimization of the Accelerating Structure

This section explains the reasoning behind the choices of the main RF features of the accelerating structure in particular the main cell geometries and the input and output power couplers. The simulation tools and procedure used to design the structure are described in detail in the CompactLight deliverable D4.1 "Report on the computer code and simulation tools which will be used for RF power unit design and cost optimization".

There are many steps in the design and optimization of a linac based on traveling-wave structures. The most important ones are [1]:

- Choose a reference value of the accelerating field.

- Define the RF power sources and pulse compressor characteristics (if foreseen).

- Set the average iris radius of the accelerating structure according to beam dynamics requirements.

- Perform the electromagnetic design and optimization of the regular, or main, cell.

- Scan the total length and the iris tapering of the structure in order to find the highest structure effective shunt impedance and then reduce the total number of power sources.

- Verify if breakdown rate predictors, like modified Poynting vector, surface electric field and pulsed heating at the nominal gradient, are below the specifications.

- Perform wakefield simulations of the accelerating structure in order to evaluate the beam breakup effects.

- Finalize the electromagnetic design of the structure including input and output couplers verifying that breakdown predictors, like pulsed heating, have acceptable values.

- Design a realistic RF module with power distribution network.

- Perform thermo-mechanical simulations of the structures and design the cooling system.

Several iterations among these steps are generally required. The first three steps are addressed in the CompactLight deliverable D2.2 "FEL design with accelerator and undulator requirements" , D4.2 "Design report of the optimized RF units" and D6.2 "Start to End simulations of the facility" respectively and specifications are given there. The subsequent steps are addressed in this document, all in this section except the last step which is described in section 3.

The workflow adopted to design and finalize the accelerating structures with cooling system is shown in Fig. 1. From the structure geometry obtained after RF system optimization, the geometry of the disks with cooling channels is designed on the basis of manufacturability principles. Then, thermo-mechanical simulations are performed and a deformed disk geometry due to heat load is obtained. A deformation model is thus derived by monitoring selected disks, in order to apply corrections to the structure geometry. The iteration process ends when the final geometry, that takes into account the heat load, matches the one designed with the electromagnetic solver.
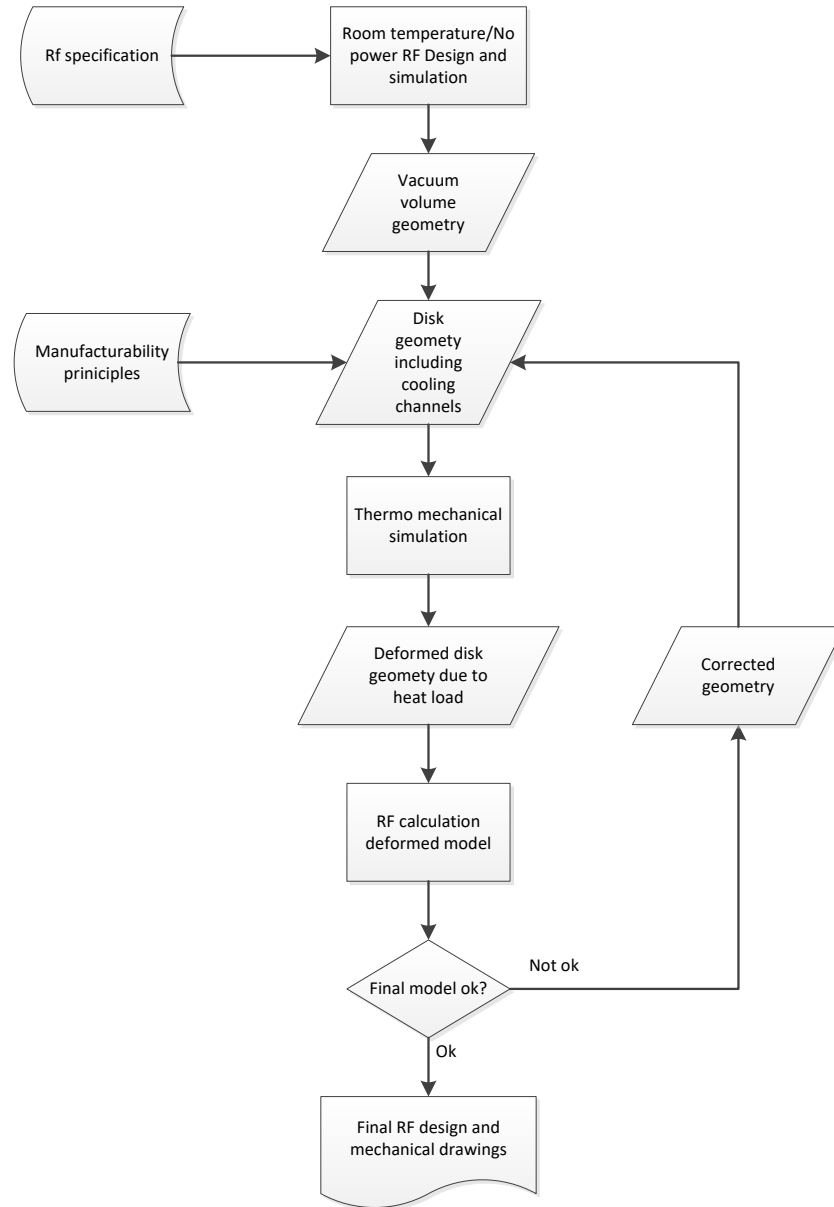
Figure 1: Workflow for the mechanical design of the accelerating structures with cooling system.

## 2.1 Design of the regular cell

The design of the regular cell has been carried out using the simulation tool ANSYS HFSS. HFSS (High Frequency Structure Simulator) [2] is a Finite Element Method (FEM) solver for electromagnetic structures from ANSYS.

A sketch of the cell geometry is shown in Fig. 2, where $a$ is the cell iris radius, $b$ the outer radius, $t$ the iris thickness, $r_0$ the radius of the cell rounding and $r_1/r_2$ is the aspect ratio of

the elliptical profile of the iris. The cell length $d$ is determined by specification of the operating frequency of 11.9942 GHz and a cell phase advance of $2\pi/3$, and is equal to 8.332 mm.
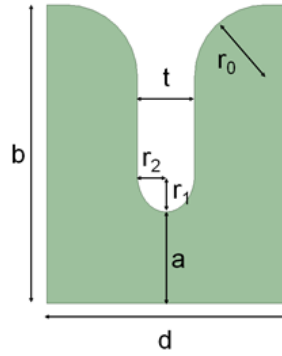


Figure 2: Sketch of the single cell with main parametrized dimensions.

The design process aimed at minimizing the modified Poynting vector normalized to the average accelerating gradient $Sc_{max}/E_{acc}^2$ while maximizing RF efficiency. The latter is quantified by the shunt impedance per unit length $R$ parameter. An elliptical shape of the irises was implemented in order to minimize the peak modified Poynting vector on its surface. It has been found that $r_1/r_2 = 1.3$ is a good compromise between expected high-gradient performance and efficiency. An $r_0$ has value equal to 2.5 mm has been chosen.

Once the iris shape was defined, the main cell parameters (shunt impedance per unit length $R$, quality factor $Q$, group velocity $v_g$, normalized modified Poynting vector $Sc_{max}/E_{acc}^2$) were calculated as a function of the iris radius $a$ and the iris thickness $t$ (Fig. 3). The $a$ value was varied in the 2 to 5 mm range, while $t$ value in the 1.5 to 2.25 mm range. On the basis of these computed parameters, it was possible to complete the design of the accelerating structures.

The data shown in Fig. 3 was then smoothed with MATLAB's [3] built-in interpolator, imposing a mesh spacing of 1 $\mu$m for both $a$ and $t$. Results are shown in Fig. 4. This interpolation allows a more precise design to be performed (see section 2.3).

## 2.2 Analytical structure length optimization

With the average iris radius of the structure defined, the first step in the design of the structure as a whole was to find the optimal length of both Constant Impedance (CI) and Constant Gradient (CG) structures. This required also simulating the the RF pulse compressor so formulas of SLED pulse compression system [4] for constant impedance and constant gradient structures [5, 6] implemented in MATLAB code were used [1, 7, 8].

The effective shunt impedance $R_s$ [6] of a pulse compressor and accelerating structure ensemble is a function of the accelerating structure attenuation $\tau_s$, the quality factor of the cell $Q$, the unloaded Q-factor of the cavities in the SLED $Q_0$, the SLED external Q-factor $Q_e$ [5, 9]. In our case, $Q$ is given by the cell design and $Q_0$ has been set equal to 180,000, as reported in [10, 11]. Thus, $R_s/R$ is only a function of $Q_e$ and $\tau_s$. The code implements the formulas described above and is able to find the value of $Q_e$ that maximise the effective shunt impedance. Once found the optimal value of $Q_e$, it is possible to find the optimal value of $\tau_s$ that maximise $R_s/R$.

(a) Shunt impedance per unit length

(b) Quality factor

(c) Group velocity

(d) Normalized modified Poynting vector
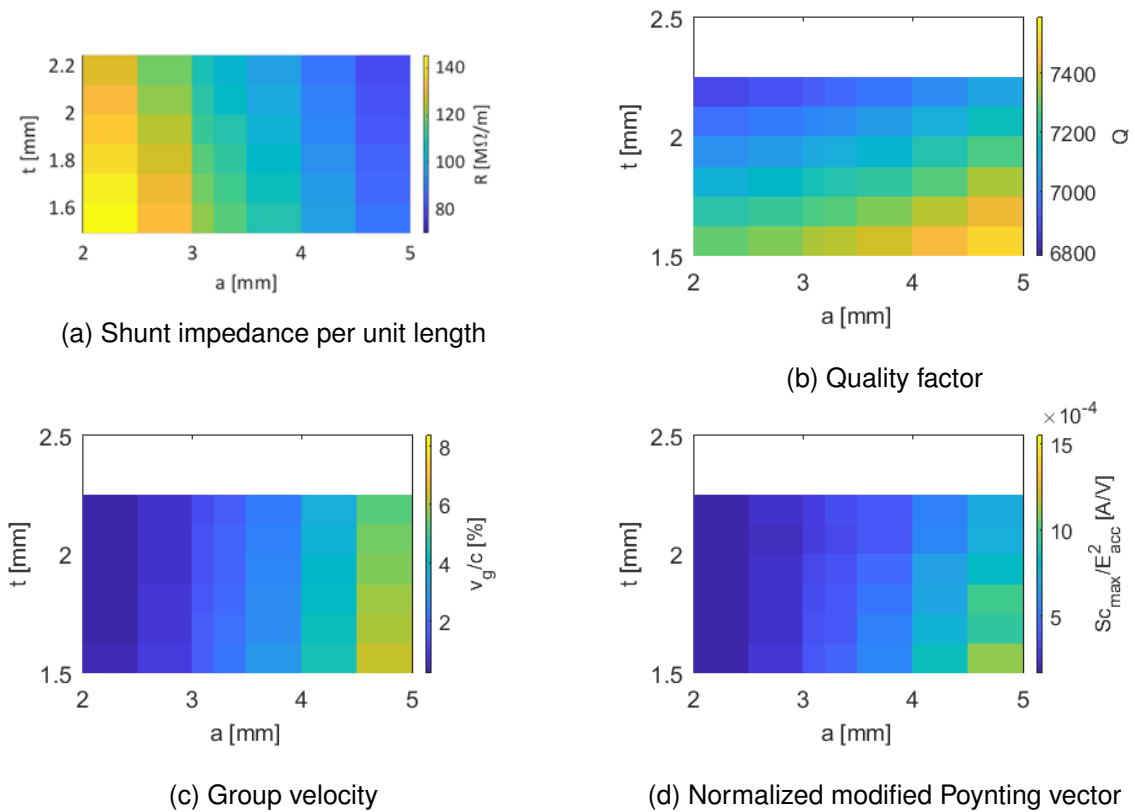
Figure 3: Main RF and geometrical parameters as a function of the iris radius and the iris thickness.

The effective shunt impedance as a function of the accelerating structure attenuation is reported in Fig. 5 for a CI and a CG structure, while the optimal structure length as function of the structure average iris aperture is reported in Fig. 6. For the CI structure the optimal length is 0.890 m while for the CG structure it is 0.818 m. These values have been used as the basis for a numerical optimization of the iris tapering as described in the following section 2.3.

## 2.3  Iris tapering

Two-bunch operation in CompactLight is needed for pump-and-probe experiments. Two-bunch operation however introduces the important design consideration of the long-range transverse wakefield behaviour of the accelerating structure. This is because the long-range transverse wakefield excited by the front bunch will affect the trajectory of the second bunch which causes an emmitance growth. Long-range transverse wakefield suppression is required, fortunately this can be achieved by a variation of the iris diameter along the length of the structure, which results in a detuning of the synchronous frequency of the most important transverse modes. This causes a decoherence in the transverse wake and thus a suppression of its amplitude [12–16].

The bunches will be separated and transferred into two FEL lines after the linac acceleration. The separation is achieved by a sub-harmonic transverse deflecting structure which is working at S-band (2.998 GHz). Thus the spacing for S-band between the two bunches should be n+0.5 rf cycles (0.5, 1.5, 2.5, etc), n is integer from 0. This results in a spacing of 2n+2 rf

(a) Shunt impedance per unit length

(b) Quality factor

(c) Group velocity

(d) Normalized modified Poynting vector
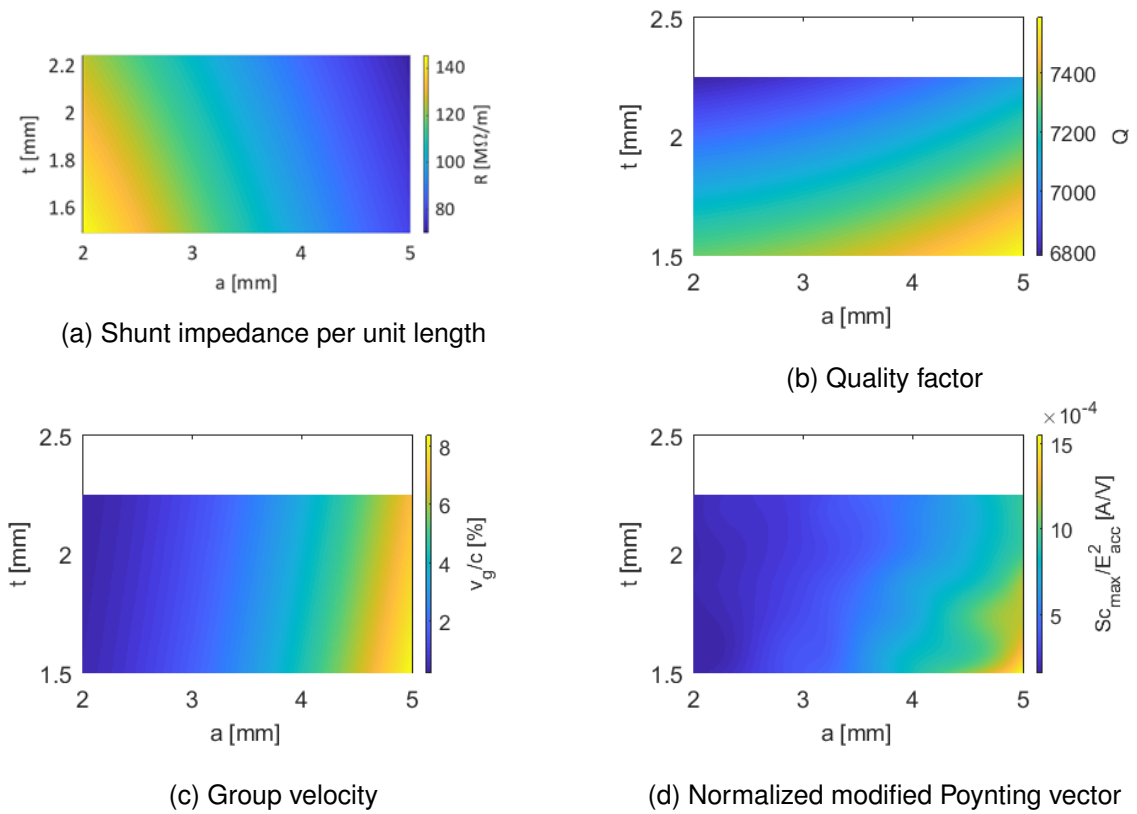
Figure 4: Main RF and geometrical parameters as a function of the iris radius and the iris thickness after interpolation with MATLAB.
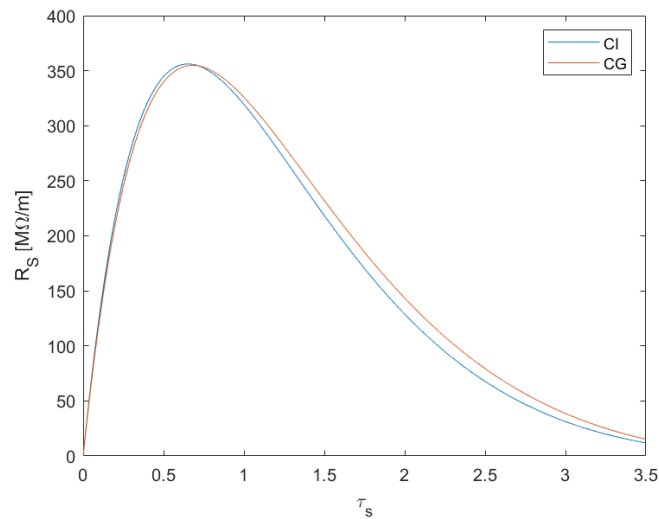


Figure 5: Effective shunt impedance as a function of the section attenuation for CI and CG structures.

cycles at X-band, n is integer from 0. The rf design of the transverse deflecting structure is presented in the CompactLight deliverable D4.2.

The initial CG design of the X-band RF structure had a linear iris aperture from 4.278 mm to
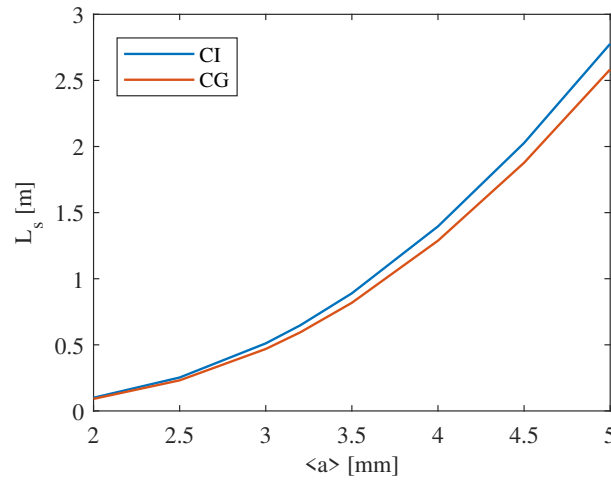
Figure 6: Optimal structure length as function of the average iris radius for CI and CG structures.

2.722 mm and a constant iris thickness of 2 mm. The long-range transverse wakefield of the linear iris design was calculated by GdfidL [17], as shown in Fig. 7. With the linear iris aperture tapering, the long-range transverse wakefield at the $4^{th}$, $6^{th}$, and $10^{th}$ rf cycle is 120, 45.83, and 18.8 V/pC/mm/m respectively.
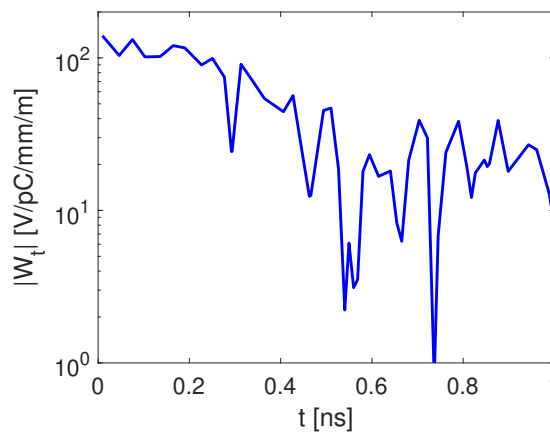


Figure 7: Long-range transverse wakefield of the initial linear iris design.

A Gaussian-like aperture tapering combined with a linear iris thickness tapering was proposed to further minimize the long-range transverse wakefield. Following a multi-parameter optimization of tapering parameters, the final iris aperture and thickness distributions are shown in Fig. 8. The blue line is the iris dimension of the linear iris design while the red line is the iris dimension of the Gaussian-like iris design.

The long-range transverse wakefield of the Gaussian-like iris design is shown in Fig. 9. The blue line is the wakefield of the linear iris design while the red line is the wakefield of the Gaussian-like iris design. The optimum compromise between fundamental-mode performance and a minimum bunch spacing distance gives a bunch spacing of $10^{th}$ RF cycle. The wakefield of the new design at the second bunch is 3.65 V/pC/mm/m. The envelope of the wakefield is
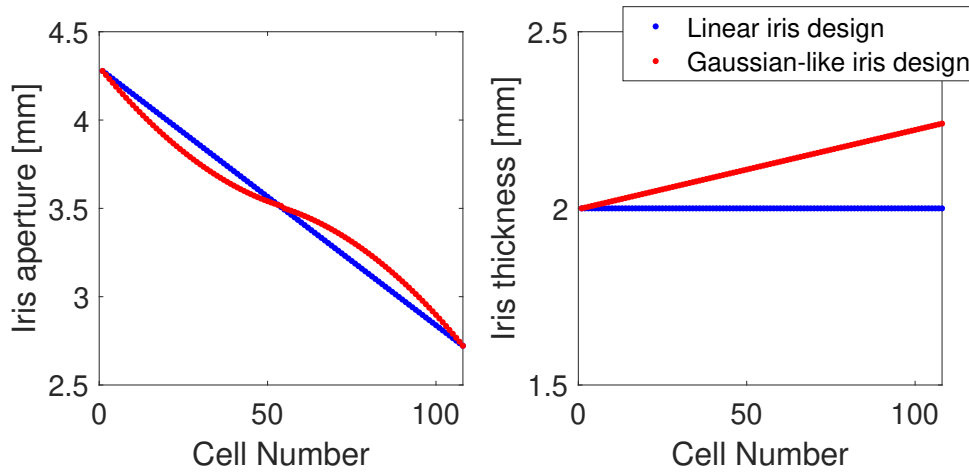
Figure 8: The iris dimension of the RF structure. Left figure is the distribution of the iris aperture. Right figure is the distribution of the iris thickness.

smaller than that of the linear iris design at the $10^{th}$ RF cycle, ensuring more robust operation.
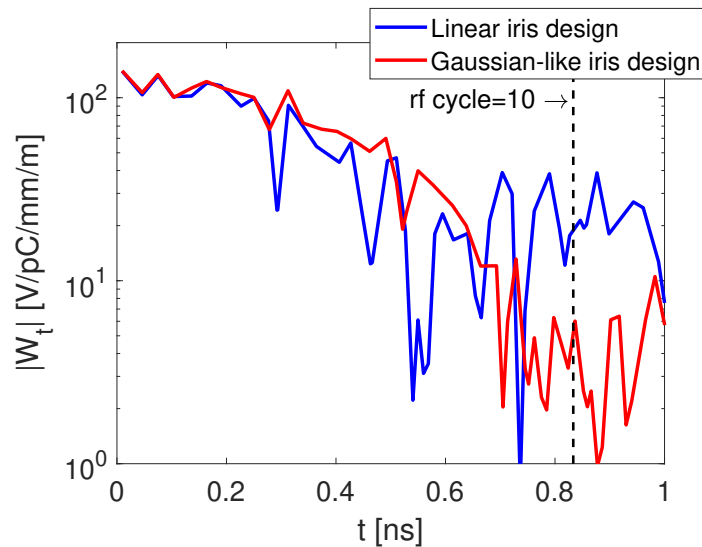


Figure 9: Long-range transverse wakefields of the initial design and the gaussian-like iris design.

## 2.4 Input and output RF power couplers

Magnetically-coupled input and output power couplers were selected because of compactness. The important design considerations for the couplers are achieving an impedance match, minimizing peak surface electric field and minimizing the quadrupolar component of the accelerating field in the structure. Critical geometrical design parameters are the radii $r_1$ and $r_2$ of the roundings between the waveguide and the slot and between the slot and the matching cell, respectively. These two radii give a geometry called z-coupling (Fig. 10). Increasing the curvature of the coupler slot reduces the surface magnetic field and thus the

pulsed heating. The radius $r_2$ has been fixed to 4 mm, while $r_1$ is 2 mm, for both the input and output couplers.
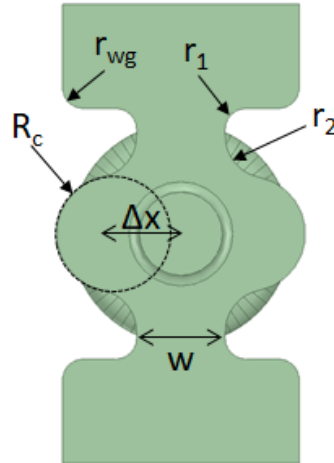


Figure 10: Detail of the RF power coupler with the main parameters.

In order to minimize the quadrupolar field component of the magnetic field, a so-called racetrack geometry has been implemented in the design. $\Delta x$ is the distance between the centre of the coupler and the centres of the semicircles with radius $R_c$. In Table 1, the main geometrical parameters of input and output couplers are reported.

Table 1: Main geometrical parameters of the RF power couplers of the X-band accelerating structures.

| Parameter | Units | Input coupler | Output coupler |
|---|---|---|---|
| Waveguide rounding $r_{wg}$ | mm | 2 | |
| Waveguide-slot rounding $r_1$ | mm | 2 | |
| Slot-matching cell rounding $r_2$ | mm | 4 | |
| Matching cell radius $R_c$ | mm | 5.063 | 6.308 |
| Off-axis circle center $\Delta x$ | mm | 8.359 | 4.765 |
| Slot width $w$ | mm | 9.017 | 7.819 |

From a scan of coupler dimensions, the obtained reflection coefficient at the the input port is -44.9 dB for the input coupler and -37. dB for the output one. For the input coupler, there is a pulsed heating of 24 °C. This value can be considered absolutely safe for high field operation.

In Fig. 11, a comparison between the couplers (with and without racetrack) is shown. Results are referenced to an arc of 2 mm radius placed at the longitudinal center of the coupler. The racetrack geometry allows the quadrupolar component of the magnetic field to be minimized. The integrated equivalent quadrupole gradient has been minimized to 4 mT, while without racetrack it is 30 mT.

## 2.5  RF module layout

From the considerations of the section 2.2 and the wakefield study, it has been found that a good compromise between RF performance and wakefield is represented by a 0.9 m structure
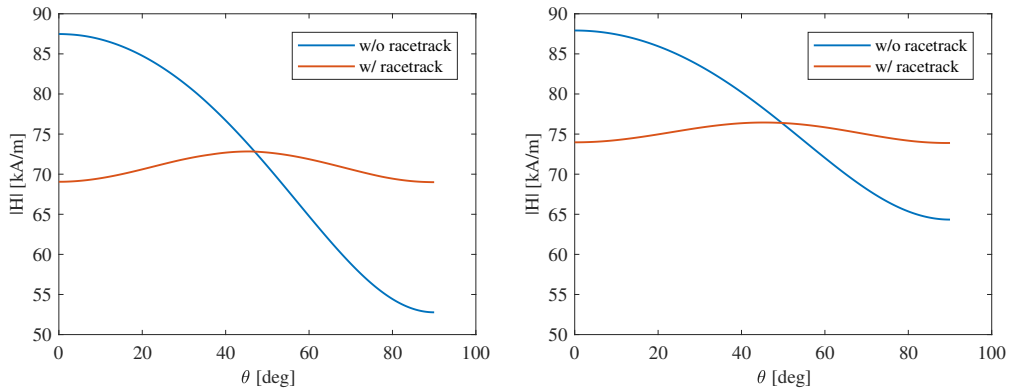
Figure 11:  Magnitude of the magnetic field in the center of the matching cell in input (left) and output (right) coupler with and without the racetrack (circle radius $r$ of 2 mm).

(109 cells) with a Gaussian profile of the iris diameter. These structures care optimally powered and assembled in a groups of four, fed by a single klystron and one SLED pulse compressor. A second klystron is added for high repetition rate operation as will be described below. This arrangement forms the RF module, a basic unit that is repeated the number of times that is necessary to achieve the desired beam energy. Full details of RF module design can be found in the CompactLight deliverable D4.2.

In Table 2, the main parameters of the structures and the module are reported while, in Fig. 12, a sketch of the RF module is shown.
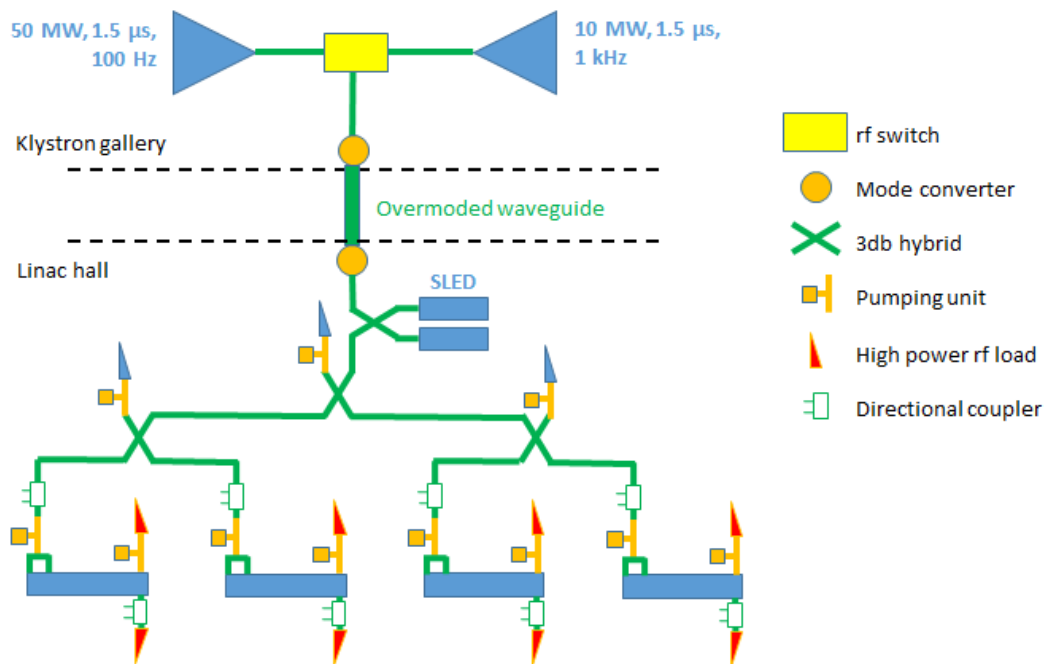


Figure 12: Sketch of the RF module.

A symmetric binary tree layout has been adopted for the power distribution. The employment

Table 2: Main parameters of the RF structures and modules

| Parameter | Units | Value | | |
|---|---|---|---|---|
| Frequency | GHz | 11.994 | | |
| Peak klystron power (100 - 250 Hz) | MW | 50 | | |
| Peak klystron power (1000 Hz) | MW | 10 | | |
| RF pulse length (250 Hz) | µs | 1.5 (0.15) | | |
| Waveguide power attenuation | % | $\approx 10$ | | |
| Average iris radius $a$ | mm | 3.5 | | |
| Iris radius $a$ | mm | 4.3-2.7 | | |
| Iris thickness $t$ | mm | 2.0-2.24 | | |
| Structure length $L_s$ | m | 0.9 | | |
| Unloaded SLED Q-factor $Q_0$ | | 180000 | | |
| External SLED Q-factor $Q_E$ | | 23300 | | |
| Shunt impedance R | $M\Omega/m$ | 85-111 | | |
| Peak modified Poynting vector | $W/\mu m^2$ | 3.4 | | |
| Group velocity $v_g/c$ | % | 4.7-0.9 | | |
| Filling time $t_f$ | ns | 146 | | |
| Repetition rate | Hz | 100 | 250 | 1000 |
| SLED | | ON | OFF | ON |
| Required klystron power | MW | 44 | 44 | 9 |
| Average accelerating gradient | MV/m | 65 | 30 | 30 |

of a circular overmoded waveguide, connecting the modulator hall with the linac hall, minimises the attenuation of power. Two mode converters are then necessary at the ends.

A 50 MW klystron is used for low repetition rate operation (100 and 250 Hz) while a 10 MW one is employed for high repetition rate operation (up to 1 kHz). The first RF source is the CPI VKX-8311A klystron [18] that is capable of providing 50 MW peak power, with a pulse length of 1.5 µs and a repetition rate of 100 Hz. This source is under routine use by the CLIC group at CERN in the XBoxes [19, 20] and will be installed at the upcoming test facility TEX at INFN-LNF in Frascati. The second source is a prototype designed by CPI or Canon that is currently still in development phase. A valid option is also represented by the Canon E37113 klystron that is able to provide 6 MW peak power, with a pulse length of 5 µs and a repetition rate of 400 Hz [21]. Also this klystron is used at CERN for the XBox-3 [22]. In this case, two klystrons of this kind are required for each RF module.

The external quality factor of the SLED has been chosen in order to maximise the RF efficiency of the module (i.e. the effective shunt impedance) while also the modified Poynting vector in the accelerating structure is well below the theoretical threshold of $4 \, W/\mu m^2$ [23]. This value should not be exceeded in order to provide stable operation at the specified accelerating gradient at a pulse length of 200 ns. In our case, the pulse length is 146 ns which gives a theoretical limit of $4.4 \, W/\mu m^2$.

The 250 Hz operating mode can be used with the baseline layout, in which only the 50 MW CPI klystrons are present. In this case, the klystron pulse is reduced to the structure filling time and the SLED is bypassed. This results in a lower input power to the accelerating structures

so this operating mode has a maximum accelerating gradient of 30 MV/m. 30 MV/m is also produced in the 1 kHz repetition rate.

The gradient profile along the structure (after one filling time) is reported in Fig. 13, while the power distribution (averaged over the pulse length and normalized to the peak value) is shown in Fig. 14.
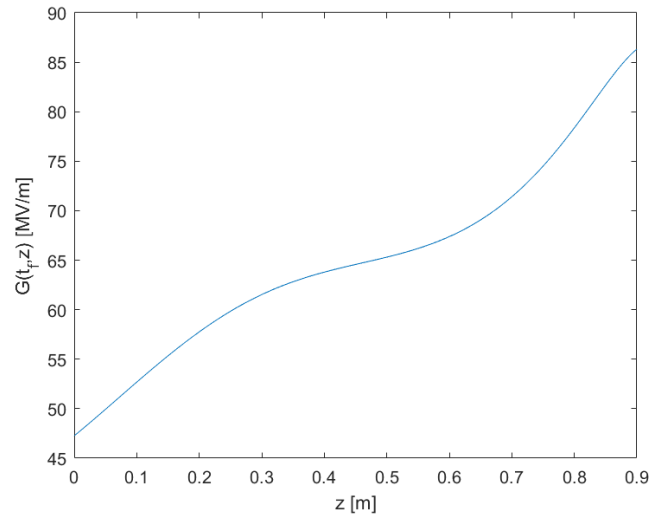


Figure 13: Accelerating gradient profile along the structure after one filling time.
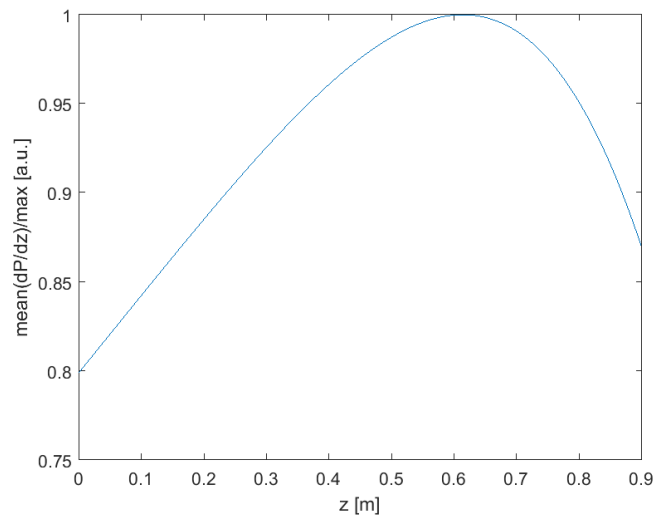


Figure 14: Power distribution (averaged over the pulse length and normalized to the peak value).

# 3  Mechanical and Thermal design

In this section the translation of the RF-volume, a result from the electromagnetic design, into a mechanical design of the RF structure is described. The result of this is the optimized design of the material (copper) surrounding the RF volume. The starting point is the RF-volume, as depicted in the left of Fig. 15. The right side of Fig. 15 shows the first iteration of the geometry of a cell into a mechanical part.
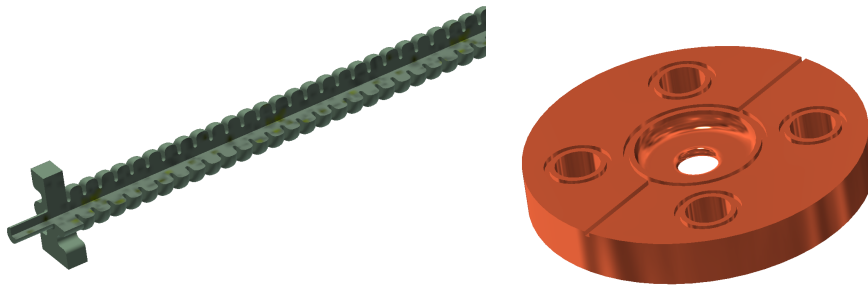


Figure 15: Three-quarter view of the Vacuum volume (Left) and initial 4-channel disc design (Right)

The mechanical considerations used during translation of the RF-volume into copper accelerating structure are listed in Table 3.

Table 3: Design assumptions used during translation of the RF-volume into copper accelerating structure.

| Assumption | Rationale |
|---|---|
| Stack of individual discs | Better machinable compared to quadrant design |
| Joining of discs to stack by brazing | Industrialized compared to diffusion bonding |
| Double "half-cell" design | Allows radius on both sides of iris |
| Internal cooling channels | Cooling channels are formed by disc stacking |

One important aspect of the optimized design comes from thermo-mechanical simulations that determine a cooling system that can handle the average thermal load during operation. The main input for the optimization is the calculated average dissipated power per structure. It is defined as the integral of the structure input power over the pulse, multiplied by the klystron repetition rate and the structure attenuation factor. The preliminary design of the cooling system has been based on 4 cooling channels distributed around the cells (see Fig. 15, right). The dimensions and the distribution of the cooling channels have been studied with a thermal analysis performed with the commercial code. In the simulation different cooling scenarios have been considered e.g. by varying the temperature, the water flux and the lengths of the channels. The maximum difference in temperature of the accelerating part of the cell is the main parameter that can contribute to the cell detuning. Therefore, deformation due to this difference in temperatures was used to gauge the results of the simulations. The design is done in two iterations with an intermediate correction of RF dimensions based on the first iteration thermal results. In the following sections the details of the studies are presented.

## 3.1 Thermo-mechanical simulations

For the baseline cooling design, a geometric design of a cell with four cooling channels is taken. Due to space constraints given by the power couplers, the cooling channels are not evenly distributed, see Fig. 16.
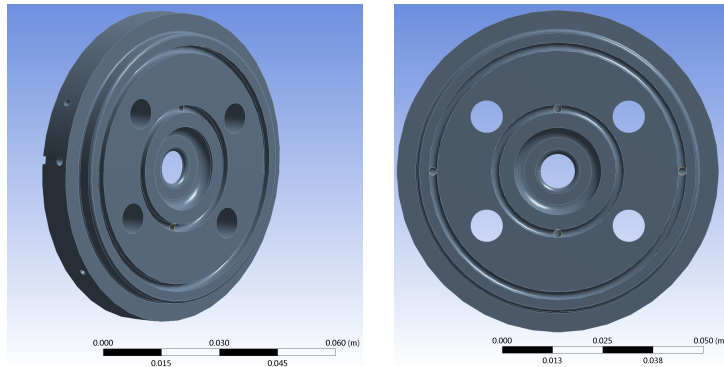


Figure 16: Geometry of disk 2 with an asymmetric cooling channel pattern

The heat transfer coefficients were calculated for a number of different scenarios; for 4, 6 and 8 mm diameter cooling channels, for 3 and 4 l/min volume flow and a channel length of 1, 2 and 4 m, respectively 4 parallel cooling channels, 2 cooling channels going back and forth (see Fig. 17) and 1 cooling channel in series over the whole structure. See Table 4 for the calculated heat transfer coefficients.
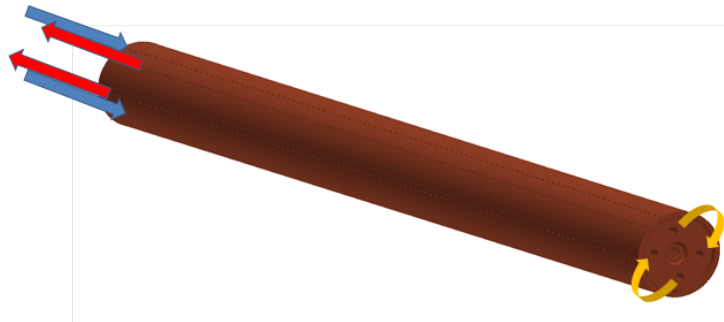


Figure 17: Route of the water flow in a structure.

To optimize the cooling geometry within the geometric boundaries, some assumptions based on reference [24] by Papke et al. were taken:

- Cooling channel diameter: 6 mm

- Symmetric routing in the structure

- Water flow: 3 l/min

- Convective heat transfer coefficient to ambient: 5 W/(m$^2$K)

- Water temperature difference max. 2 $^\circ$C

Table 4: Heat transfer coefficients

| d cooling [mm] | l cooling [m] | flow [l/min] | heat transfer coefficient [W/(m$^2$K)] |
|:---:|:---:|:---:|:---:|
| 4 | 1 | 3 | 12000 |
| 6 | 1 | 3 | 6500 |
| 8 | 1 | 3 | 4100 |
| 4 | 2 | 3 | 8850 |
| 6 | 2 | 3 | 5000 |
| 8 | 2 | 3 | 3300 |
| 4 | 4 | 3 | 5775 |
| 6 | 4 | 3 | 3450 |
| 8 | 4 | 3 | 2365 |
| 4 | 1 | 4 | 15500 |
| 6 | 1 | 4 | 8250 |
| 8 | 1 | 4 | 5250 |
| 4 | 2 | 4 | 11500 |
| 6 | 2 | 4 | 6450 |
| 8 | 2 | 4 | 4250 |

- Water cooling heat transfer coefficient: 5 kW/(m$^2$K)

- Water inlet temperature: 30 $^\circ$C

- Water outlet temperature: 32 $^\circ$C

- Room temperature: 22 $^\circ$C

- Water pressure: 6*10$^5$ Pa

For 3 l/min and a 2 times back-and-forth routing (see Fig. 17, the heat transfer coefficient was calculated to be 5000 W/(m$^2$K), the same number as was used in the calculations by Papke [24]. Interesting to note is the mention of the significant impact by surface roughness of the cooling pipes. A conservative number was used, so the heat transfer coefficient could be improved by roughening the cooling channels.

With these inputs and the worst case heat load provided by the RF calculations (1000 Hz repetition rate leading to 2.2 kW dissipated power in the structure), the temperature profile and respective deformation of three disks are calculated: disk nr. 2, 54 and 106, see Fig. 18 and Fig. 19.

The deformation is mostly caused by the difference between the operating temperature and the temperature at which the disks were made and measured (20 $^\circ$C). Therefor also the deformation due to the temperature difference within a disk is shown in Fig. 20. The results are summarized in Table 5.

**Conclusions**

With the power distribution from the RF calculations (1000 Hz rep rate, 2.2 kW over the structure), the temperature distribution in three disks across the accelerator was calculated. From
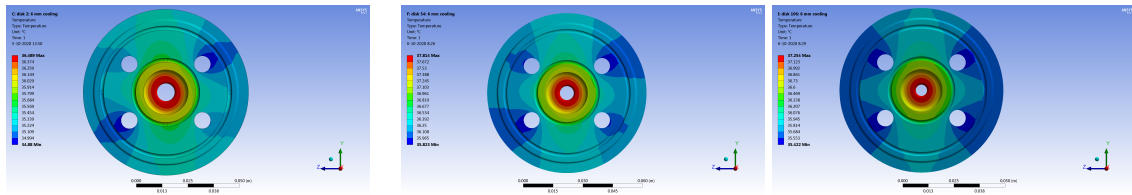
Figure 18: The temperature profile of disk 2, 54 and 106.
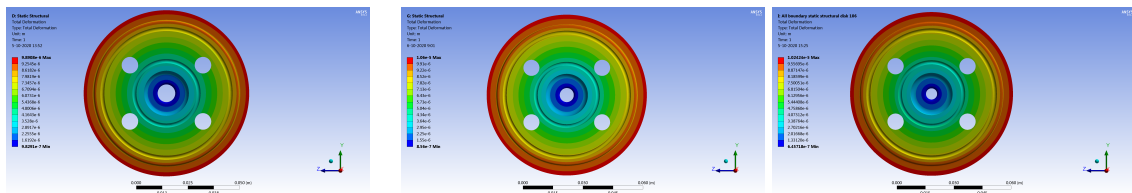


Figure 19: The total deformation of disk 2, 54 and 106.
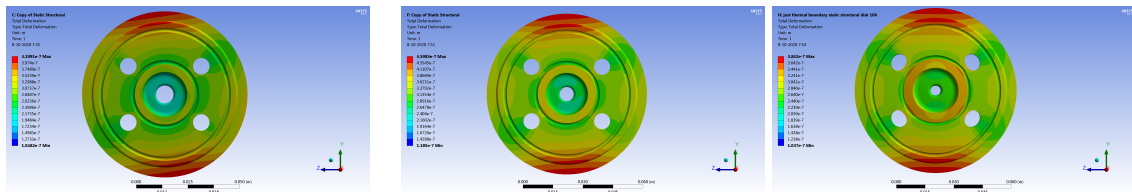


Figure 20: The deformation of disk 2, 54, and 106, if only the temperature difference in the disk is taken into account.

Table 5: Results of the temperature and deformation

| | Temperature min - max ($\Delta T$) [$^{\circ}$C] | Deformation due to temperature difference within the disk $\mu$m | Total deformation $\mu$m |
|---|---|---|---|
| Disk 2 (3 l/min ) | 34.9 - 36.5 (1.61) | 0.11 - 0.42 | 0.98 - 9.9 |
| Disk 54 (3 l/min ) | 35.8 - 37.8 (1.99) | 0.12 - 0.46 | 0.86 - 10.6 |
| Disk 106 (3 l/min ) | 35.4 37.3 (1.83) | 0.10 - 0.38 | 0.65 - 10.2 |
| Disk 106 (4 l/min ) | 35.4 - 36.2 (0.80) | 0.10 - 0.38 | 0.59 - 9.45 |

the temperature profile and the water pressure, the deformation was calculated and shown. The deformation is dominated by difference in water temperature (30 $^{\circ}$C) and the temperature when the parts were made (20 $^{\circ}$C). This deformation can be corrected by adjusting the dimensions of the cavity disks. This will need to be finalised when the working temperature (i.e. water temperature) is decided. Therefore, also the deformation in the disk is shown even if only the temperature difference over the disk is taken into account. The total deformation in the iris is uniform and less than 1 $\mu$m. The maximum deformation due to the temperature difference in the disk itself is approximately 0.5 $\mu$m. The difference in deformation is about

10% between 3 and 4 l/min water flow.

## 3.2 Second iteration after RF verification

After verification by the RF, a second iteration of the simulations was done, again for 1000 Hz repetition rate case. This iteration included variable thickness of the cavities and additional details like thermocouple channels. The results from the study are presented in Table 6. A detailed drawings can be produced after that step. An example of a typical design drawings of the cavity cells are shown in Fig. 21.

Table 6: Results after RF verification

|  | **Temperature min - max ($\Delta T$) [$^\circ$C]** | **Deformation due to temperature difference with the disk $\mu$m** | **Total deformation $\mu$m** |
|---|---|---|---|
| Disk 2 | 36.5 - 38.1 (1.6) | 0.10 - 0.40 | 1.09 - 11.1 |
| Disk 54 | 37.7 - 39.7 (2.0) | 0.12 - 0.48 | 0.97 - 12.0 |
| Disk 106 | 37.1 - 38.9 (1.8) | 0.11 - 0.41 | 0.73 - 11.5 |

**Conclusions**

In the second iteration with added variable thickness and updated geometry, and with the same heat load (1000 Hz rep rate, 2.2 kW over the structure), the temperature and deformations were calculated. The deformation increased slightly, but can be corrected if the dimensions are adjusted for the operating temperature. The deformation due to the temperature difference in the disk itself is still approx. 0.5 $\mu$m.

## 3.3 Lower heat load, 100 Hz repetition rate

The heat load for the 100 Hz has also been modelled. The heat load for this case is 1000 W over the structure and the same heat load profile, as in the high rep rate, was assumed. The starting point for these analyses was the deformation in the centre to be as close as possible to the high repetition rate case. To realise this, the cooling water temperature has been raised from 30 $^\circ$C to 34.5 $^\circ$C, in order to match the temperature in the centre of the iris. This leads to an optimum, as the temperatures in the middle could not be precisely met by one temperature raise, as can be seen in Table 7.

The consequence of the lower power in combination with the higher water temperature is that the temperature at the edge is higher. This results in more expansion of the disk towards the edge. This should also be kept in mind for the structure support and alignment. An alternative is to decrease the water flow, but with the current flow (3 l/min), it would be close to becoming laminar, so this is not advised.

In the last column of Table 7, the difference in deformation at the cell location is shown. These are all positive, as the temperature towards the edge is higher due to the higher water temperature. The optimization is done for the iris location, so the deformation at the cell

| Disk | xx | yy | zz | e_a | e_b |
|---|---|---|---|---|---|
| 1 | 21.74577516 | 8.557857932 | 21.74577516 | 1.3 | 1 |
| 2 | 21.74577516 | 8.512405822 | 21.7301134 | 1.301457944 | 1.001121495 |
| 3 | 21.7301134 | 8.467593304 | 21.71095286 | 1.302915888 | 1.002242991 |
| 4 | 21.71095286 | 8.423420376 | 21.69256133 | 1.304373832 | 1.003364486 |
| 5 | 21.69256133 | 8.37988704 | 21.67427645 | 1.305831776 | 1.004485981 |
| 6 | 21.67427645 | 8.336993296 | 21.65631869 | 1.30728972 | 1.005607477 |
| 7 | 21.65631869 | 8.294739142 | 21.63846742 | 1.308747664 | 1.006728972 |
| 8 | 21.63846742 | 8.25312458 | 21.62136712 | 1.310205607 | 1.007850467 |
| 9 | 21.62136712 | 8.212149609 | 21.60480158 | 1.311663551 | 1.008971963 |
| 10 | 21.60480158 | 8.171814229 | 21.58811399 | 1.313121495 | 1.010093458 |
| 11 | 21.58811399 | 8.13211844 | 21.5719508 | 1.314579439 | 1.011214953 |
| 12 | 21.5719508 | 8.093062243 | 21.5565223 | 1.316037383 | 1.012336449 |
| 13 | 21.5565223 | 8.054645637 | 21.54118663 | 1.317495327 | 1.013457944 |
| 14 | 21.54118663 | 8.016868622 | 21.52613799 | 1.318953271 | 1.014579439 |
| 15 | 21.52613799 | 7.979731198 | 21.51159537 | 1.320411215 | 1.015700935 |
| 16 | 21.51159537 | 7.943233366 | 21.4973531 | 1.321869159 | 1.01682243 |
| 17 | 21.4973531 | 7.907375125 | 21.48360577 | 1.323327103 | 1.017943925 |
| 18 | 21.48360577 | 7.872156475 | 21.46971579 | 1.324785047 | 1.019065421 |
| 19 | 21.46971579 | 7.837577416 | 21.45630868 | 1.326242991 | 1.020186916 |
| 20 | 21.45630868 | 7.803637948 | 21.44360069 | 1.327700935 | 1.021308411 |
| 21 | 21.44360069 | 7.770338072 | 21.43096005 | 1.329158879 | 1.022429907 |
| 22 | 21.43096005 | 7.737677787 | 21.41856573 | 1.330616822 | 1.023551402 |
| 23 | 21.41856573 | 7.705657093 | 21.40663419 | 1.332074766 | 1.024672897 |
| 24 | 21.40663419 | 7.674275599 | 21.39498187 | 1.33353271 | 1.025794393 |
| 25 | 21.39498187 | 7.643534479 | 21.38378213 | 1.334990654 | 1.026915888 |
| 26 | 21.38378213 | 7.613432559 | 21.37280962 | 1.336448598 | 1.028037383 |
| 27 | 21.37280962 | 7.58397023 | 21.36188636 | 1.337906542 | 1.029158879 |
| 28 | 21.36188636 | 7.555147492 | 21.35162352 | 1.339364486 | 1.030280374 |
| 29 | 21.35162352 | 7.526964346 | 21.34179608 | 1.34082243 | 1.031401869 |
| 30 | 21.34179608 | 7.49942079 | 21.33178869 | 1.342280374 | 1.032523364 |
| 31 | 21.33178869 | 7.472516826 | 21.32182218 | 1.343738318 | 1.03364486 |
| 32 | 21.32182218 | 7.446252454 | 21.31250137 | 1.345196262 | 1.034766355 |
| 33 | 21.31250137 | 7.420627672 | 21.30360212 | 1.346654206 | 1.035887855 |
| 34 | 21.30360212 | 7.395642482 | 21.29489793 | 1.34811215 | 1.037009346 |
| 35 | 21.29489793 | 7.371296883 | 21.28660672 | 1.349570093 | 1.038130841 |
| 36 | 21.28660672 | 7.347590875 | 21.27856315 | 1.351028037 | 1.039252336 |
| 37 | 21.27856315 | 7.324524458 | 21.27054677 | 1.352485981 | 1.040373832 |
| 38 | 21.27054677 | 7.302097633 | 21.26271498 | 1.353943925 | 1.041495327 |
| 39 | 21.26271498 | 7.280310399 | 21.2552852 | 1.355401869 | 1.042616822 |
| 40 | 21.2552852 | 7.259162756 | 21.24825288 | 1.356859813 | 1.043738318 |
| 41 | 21.24825288 | 7.238654704 | 21.24145943 | 1.358317757 | 1.044859813 |
| 42 | 21.24145943 | 7.218786243 | 21.23505764 | 1.359775701 | 1.045981308 |
| 43 | 21.23505764 | 7.199557374 | 21.22882894 | 1.361233645 | 1.047102804 |
| 44 | 21.22882894 | 7.180968096 | 21.22261443 | 1.362691589 | 1.048224299 |
| 45 | 21.22261443 | 7.163018409 | 21.21700389 | 1.364149533 | 1.049345794 |
| 46 | 21.21700389 | 7.145708314 | 21.21140603 | 1.365607477 | 1.05046729 |
| 47 | 21.21140603 | 7.129037809 | 21.20597323 | 1.367065421 | 1.051588785 |
| 48 | 21.20597323 | 7.113006896 | 21.20092125 | 1.368523364 | 1.05271028 |
| 49 | 21.20092125 | 7.097615574 | 21.19609473 | 1.369981308 | 1.053831776 |
| 50 | 21.19609473 | 7.082863844 | 21.19164511 | 1.371439252 | 1.054953271 |
| 51 | 21.19164511 | 7.068751704 | 21.18735504 | 1.372897196 | 1.056074766 |
| 52 | 21.18735504 | 7.055279156 | 21.18307166 | 1.374355164 | 1.057196262 |
| 53 | 21.18307166 | 7.042446199 | 21.17900977 | 1.375813084 | 1.058317757 |
| 54 | 21.17900977 | 7.030252833 | 21.17531982 | 1.377271028 | 1.059439252 |
| 55 | 21.17531982 | 7.001163224 | 21.1688664 | 1.378728972 | 1.060560748 |
| 56 | 21.1688664 | 6.9884414 | 21.16205688 | 1.380186916 | 1.061682243 |
| 57 | 21.16205688 | 6.97507978 | 21.15838871 | 1.38164486 | 1.062803738 |
| 58 | 21.15838871 | 6.961078367 | 21.15472615 | 1.383102804 | 1.063925234 |
| 59 | 21.15472615 | 6.946437159 | 21.15012994 | 1.384560748 | 1.065046729 |
| 60 | 21.15012994 | 6.931156156 | 21.14554111 | 1.386018692 | 1.066168224 |
| 61 | 21.14554111 | 6.915235359 | 21.14117354 | 1.387476636 | 1.06728972 |
| 62 | 21.14117354 | 6.898674768 | 21.13645311 | 1.388934579 | 1.068411215 |
| 63 | 21.13645311 | 6.881474382 | 21.13117064 | 1.390392523 | 1.06953271 |
| 64 | 21.13117064 | 6.863634202 | 21.12554081 | 1.391850467 | 1.070654206 |
| 65 | 21.12554081 | 6.845154227 | 21.12013627 | 1.393308411 | 1.071775701 |
| 66 | 21.12013627 | 6.826034458 | 21.11438938 | 1.394766355 | 1.072897196 |
| 67 | 21.11438938 | 6.806274895 | 21.1080917 | 1.396224299 | 1.074018692 |
| 68 | 21.1080917 | 6.785875537 | 21.10181404 | 1.397682243 | 1.075140187 |
| 69 | 21.10181404 | 6.764836384 | 21.09576687 | 1.399140187 | 1.076261682 |
| 70 | 21.09576687 | 6.743157437 | 21.08938878 | 1.400598131 | 1.077383178 |
| 71 | 21.08938878 | 6.720838696 | 21.0824734 | 1.402056075 | 1.078504673 |
| 72 | 21.0824734 | 6.69788016 | 21.07523713 | 1.403514019 | 1.079626168 |
| 73 | 21.07523713 | 6.67428183 | 21.06768403 | 1.404971963 | 1.080747664 |
| 74 | 21.06768403 | 6.650043705 | 21.06037595 | 1.406429907 | 1.081869159 |
| 75 | 21.06037595 | 6.625165786 | 21.05310563 | 1.40788785 | 1.082990654 |
| 76 | 21.05310563 | 6.599648073 | 21.04532355 | 1.409345794 | 1.08411215 |
| 77 | 21.04532355 | 6.573490565 | 21.03724345 | 1.410803738 | 1.085233645 |
| 78 | 21.03724345 | 6.546693262 | 21.02942069 | 1.412261682 | 1.08635514 |
| 79 | 21.02942069 | 6.519256165 | 21.02131275 | 1.413719626 | 1.087476636 |
| 80 | 21.02131275 | 6.491179274 | 21.0127181 | 1.41517757 | 1.088598131 |
| 81 | 21.0127181 | 6.462462588 | 21.00385559 | 1.416635514 | 1.089719626 |
| 82 | 21.00385559 | 6.433106108 | 20.9952683 | 1.418093458 | 1.090841121 |
| 83 | 20.9952683 | 6.403109833 | 20.98675596 | 1.419551402 | 1.091962617 |
| 84 | 20.98675596 | 6.372473764 | 20.97746073 | 1.421009346 | 1.093084112 |
| 85 | 20.97746073 | 6.341197901 | 20.96824706 | 1.42246729 | 1.094205607 |
| 86 | 20.96824706 | 6.309282243 | 20.95932335 | 1.423925234 | 1.095327103 |
| 87 | 20.95932335 | 6.276726791 | 20.95015764 | 1.425383178 | 1.096448598 |
| 88 | 20.95015764 | 6.243531544 | 20.94054897 | 1.426841121 | 1.097570093 |
| 89 | 20.94054897 | 6.209696502 | 20.93070395 | 1.428299065 | 1.098691589 |
| 90 | 20.93070395 | 6.175221667 | 20.92114011 | 1.429757009 | 1.099813084 |
| 91 | 20.92114011 | 6.140107036 | 20.91133982 | 1.431214953 | 1.100934579 |
| 92 | 20.91133982 | 6.104352612 | 20.90109968 | 1.432672897 | 1.102056075 |
| 93 | 20.90109968 | 6.067958393 | 20.89092118 | 1.434130841 | 1.10317757 |
| 94 | 20.89092118 | 6.030924379 | 20.88100829 | 1.435588785 | 1.104299065 |
| 95 | 20.88100829 | 5.993250571 | 20.87084998 | 1.437046729 | 1.105420561 |
| 96 | 20.87084998 | 5.954936069 | 20.86024309 | 1.438504673 | 1.106542056 |
| 97 | 20.86024309 | 5.915983572 | 20.84939483 | 1.439962617 | 1.107663551 |
| 98 | 20.84939483 | 5.876390381 | 20.83880221 | 1.441420561 | 1.108785047 |
| 99 | 20.83880221 | 5.836157395 | 20.82797881 | 1.442878505 | 1.109906542 |
| 100 | 20.82797881 | 5.795284615 | 20.8167293 | 1.444336449 | 1.111028037 |
| 101 | 20.8167293 | 5.75377204 | 20.80555469 | 1.445794393 | 1.112149533 |
| 102 | 20.80555469 | 5.711619671 | 20.79435989 | 1.447252336 | 1.113271028 |
| 103 | 20.79435989 | 5.668827508 | 20.783246 | 1.44871028 | 1.114392523 |
| 104 | 20.783246 | 5.625395505 | 20.77173867 | 1.450168224 | 1.115514019 |
| 105 | 20.77173867 | 5.581323797 | 20.76003937 | 1.451626168 | 1.116635514 |
| 106 | 20.76003937 | 5.536612251 | 20.74862998 | 1.453084112 | 1.117757009 |
| 107 | 20.74862998 | 5.491260909 | 20.73704529 | 1.454542056 | 1.118878505 |
| 108 | 20.73704529 | 5.445269774 | 20.72937303 | 1.456 | 1.12 |

Figure 21: Typical drawings of the cavities (top), coupler (bottom left) and endcap (bottom right)

location will be higher in the 100 Hz case. A different choice could of course be made for the optimization strategy.

**Conclusions**

An optimization is done to minimize the difference in temperature (and therefore deformation) at the iris of the disks for the 100 Hz repetition rate. The heat load of 1000 W (instead of 2.2 kW) with the same distribution profile was used, and the water temperature was raised to compensate for the lower heat load. The water temperature of 34.5 °C leads to the same temperature at the iris for the last disks in the structure, but at the beginning of the structure the temperature is 0.4 °C higher, while in the middle of the structure the temperature at the iris is 0.4 °C lower.

The difference in deformation between the 1000 Hz and the 100 Hz case with the higher

Table 7: Result of the temperature optimization at the location of the iris, by raising the water temperature

|  | Temperature 1000 Hz [$^o$C] | Temperature 100 Hz [$^o$C] | Temperature difference [$^o$C] | Deformation difference at cell location [$\mu$m] |
|---|---|---|---|---|
| Disk 2 | 38.1 | 38.5 | 0.4 | 0.15 |
| Disk 54 | 39.7 | 39.3 | - 0.4 | 0.05 |
| Disk 106 | 38.9 | 38.9 | 0.0 | 0.08 |

cooling water temperature at the cell location is less than $0.2\,\mu$m.

# 4 Industrialization

In this section the route towards an industrialization of the accelerator section will be described based on a breakdown of the various production processes. The intent is to give general statements that are founded on commonly available ideas, approaches and developments in industry. Nevertheless, a slight bias towards the preferences of a manufacturer cannot be ruled out. As there are various potential routes that can lead to the same functional product, the specific approach chosen by a given manufacturer is influenced by the exact type of machines, knowledge and experiences gained in the past.

## 4.1 Challenges

The goal is to produce an entire accelerator section within tolerance for minimum costs with a short lead-time. In order to do so, the production process has to be of an industrialized level with e.g. low reject rate, high degree of mechanisation/automation and a high degree of reproducibility.

The challenges in the industrialization of accelerator structures are predominantly in the (sub)micrometer-machining of the copper parts and the consecutive assembly of the accelerator section due to the very strict mechanical tolerances. In state-of-the-art X-band designs these tolerances are approaching the limits of machining techniques available to date.

The typical work-flow of high precision monoparts is as follows:

- Production of bulk material

- Pre-machining

- Thermal annealing

- Final-machining

- Metrology

- Cleaning

- Packaging

As the final machining steps are (absolutely as well as relative) the most time- and cost-consuming, it is important to minimize the amount of material allowance after pre-machining. By this, the final machining can be done in a limited number of passes i.e. number of times the tool moves across the material for the consecutive material removal. This optimization has to be done throughout the entire production chain i.e. from raw material until final product. The production of the bulk material is not in the scope of this study as this is produced according to international standards and can be procured as such.

## 4.2 Pre-machining

After cutting the raw material (typically bar stock) into individual blanks, the bulk material removal is done during pre-machining by so called high-precision technology machines i.e. machines capable of manufacturing parts reproducible with an accuracy of $10\,\mu m$.

As mentioned above, also pre-machining has to be done in a specific and reproducible manner in order to reduce the number of final-machining steps. The machining of the material has to be done such that the amount of stress introduced in the material is low and especially reproducible. By this it is assured that the residual stress is below a critical value after annealing, such that the parts remain within the desired specification after this stress is released during final-machining. Another point of attention is the handling of the material. Rough handling e.g. stacking semi-finished products in transport containers might dent, scratch or deform the soft copper material in such a severe way that these defect cannot be removed by final machining. Where these defects are easily recognizable by visual inspection, stress that is introduced into the product is hardly detectable.

Despite recent innovations in machine development, currently available High-Precision Technology (HPT) machines that employ cemented carbide tools, are not yet able to achieve the desired surface roughness of the parts. In order to achieve these low roughness values, the final machining has to be done by using single point diamond tipped tools. Nevertheless, developments and improvements of these techniques is continued in order to balance the ratio between pre- and final-machining even further.

## 4.3 Thermal annealing

Even after careful pre-machining, there will be some stress in the material that needs to be relieved before final-machining. If not, this stress can cause deformation of the parts during the joining of the parts by brazing techniques due to the elevated temperature.

Typically, the stress in the material is released by thermal annealing i.e. controlled heating of the material to a certain temperature, maintaining that temperature for a given time, followed by a controlled cool-down back to room temperature. To prevent oxidation of the surface, annealing is done under vacuum. This is especially important if not all surfaces are final-machined i.e. when some final dimensions are produced by the pre-machining steps. Otherwise, these surfaces will heavily oxidize which hampers joining the parts by brazing. Depending on the desired outcome, the temperature profile (ramp-up, holding and ramp-down) is to be optimized.

As the annealing process not only releases stress in the material, it also changes the material on a microscopic level i.e. the grain-size and its distribution is also affected by the annealing process. As the grain-size influences the rate of tool wear, this effect should also be taken into account in the optimization, as tool wear introduces extra costs for tool replacement. Furthermore, tool wear during machining leads to a less defined manufacturing process that leads to a wider tolerance range. Experiences in the past learn that a single annealing step at 240 °C yields the best combined result in stress relief and grain dimensions.

## 4.4 Final machining

Typically, the final machining consists of alternating machining and measurement steps, in order to assure product quality. Furthermore, the cleanliness of the parts is of high importance as contamination of the parts will lead to contamination of the vacuum-system they are used in. This cleanliness gives also some boundaries to the use of cooling liquid during machining. As the parts have to be free of sulphur and chlorine, these elements are not allowed to be present in any of the machining steps.

### 4.4.1 Single point diamond machining

Where normal machine tools are made of tungsten carbide, the cutting edge of the tools used for final machining the high purity (> 99.99%) oxygen free copper are based on diamond. These so-called single point diamond tools allow to machine the soft copper with a high accuracy combined with a mirror finished surface.

The machining steps can be separated in two distinct groups i.e. milling and turning. In a milling operation, the machine tool rotates and removes material in an intermittent behaviour i.e. each revolution of the tool a small chip of material is removed. In a turning operation, the part rotates and the machine tool remains in contact with the part and a continuous ribbon-like stream of material is removed. Due to this difference in nature, a turning operation results in a surface roughness that is about five to ten times lower compared to a milled surface. Hence, it is preferred to machine as little as possible by milling.

### 4.4.2 Metrology

During and after machining parts need to be measured to ensure that the final part is within specification. Depending on the stability of the production process, the interval at which parts are to be measured can vary from 100% for very critical dimensions down to 1-in-4 or even 1-in-8 for less critical dimensions or dimensions machined by the very stable turning operation.
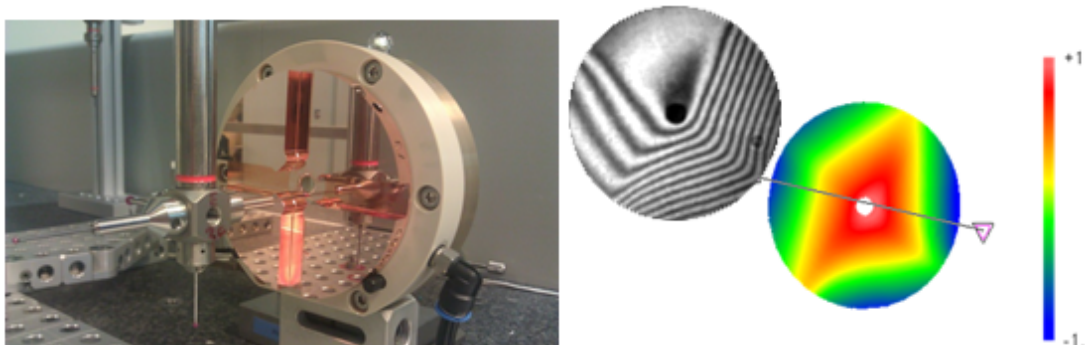


Figure 22: Geometrical measurement on a 3D CMM (left) and flatness measurement by light interferometry (Right)

Form and position tolerances on the part are in region of 1 to 2 $\mu$m and need to be measured with a touch probe (Fig. 22 left) of a coordinate-measuring machine (CMM). Measuring forces need to be much lower than normally can be expected on the CMM as no metrology marks can be left on the surface. Parts need to be as flat as possible (below 1-2 $\mu$m). Interferometer measurements are used to measure the flatness of parts (Fig. 22 right). Surface finish needs to be in the region of a 5 to 25 nm and needs to be measured with a white light interferometer.

### 4.4.3 Cleaning

The parts have to be ultra clean and this has to be kept in mind during the entire manufacturing process. To avoid all possible scratches on the parts gloves need to be worn during pre- and end-machining. Cutting fluids need to be free of chlorine or sulphur as this can contaminate the RF function of the parts. Cutting fluids used in the process need to be removed so an

ultrasonic cleaning method, followed by a vapor degreasing step, again with solvents that do not contain sulphur or chlorine. Given the very fragile (high risk of denting/bending/scratching) special holding tools need to be developed in order to hold the parts during the cleaning steps. After cleaning, the packaging and storage has to be such that the parts will not oxidize and/or become damaged during handling, transport and storage.

### 4.4.4 Joining techniques

Individual machined parts need to be joined into (sub)assemblies that form the accelerator structure. As the RF components need to be used in a vacuum environment, the assemblies have to be vacuum tight. In order to achieve this, all the seams between the parts have to be closed. There are a few techniques that are used e.g. vacuum brazing, diffusion bonding, (e-beam) welding, bolt-connection with sealing material between the parts.

Bolt-connections are typically used to join larger sub-assemblies together via tubes/pipes by means of standardized flanges and gaskets. Due to their nature, bolt-connections can be made without any specialized tools on site of installation. Furthermore they are reversible, which allows to service/replace sub-assemblies. Major drawback is that these connections are less vacuum tight compared to other techniques.

Welding is a technique that joints metals parts together by locally melting the material on both sides of the seam. Upon solidification of weld pool, a material continuum is created. Materials on both sides of the seam have to be similar (or at least very alike). The heating can be done by various means including an electric arc or high energy electron beam. Depending on the width of the seam, filler material of similar composition as the base material can be added when melting of the base material is not sufficient to form the weld pool. In accelerator applications, welding is typically used for joining stainless steel parts together. In a limited application, electron beam welding is used to weld copper parts together.

Where additional filler material is optional in a welding process, it is essential in a brazing process. Here, the seam between the metal parts is closed by melting a filler material that has a lower melting temperature than the base materials. In contrast to a welding process, the base material is not melted which allows upon careful selection of the filler material to join dissimilar metals. Soldering is a low-temperature analog to brazing which is typically used for cooling pipes and electrical connections. The heat necessary to melt the filler material can be applied by various means including electric current, open gas flame, (vacuum)oven. In accelerator applications brazing is typically performed in vacuum ovens in order to apply the temperature evenly and under a controlled atmosphere to avoid oxidation of the parts. In this particular application, the filler material is stacked between the parts in form of wire or thin sheets. The parts and their assembly need to be designed towards the brazing process in which on has to take care that the filler material is flowing only into the zones in which brazing is foreseen. Ill designed parts and/or wrong amount of filler material can lead to spills and/or vacuum leaks. Using different types of filler material, each with a different melting temperature allows to braze complex assemblies in multiple steps, further optimizing the final result. As with welding, brazing is a non-reversible technique i.e. parts cannot be dismounted without applying a cutting technique which removes material at the location of the seam.

Diffusion bonding is a technique in which similar metal parts are joined together by applying substantial force on the parts while heating them to just below the melting temperature in a controlled atmosphere. During this operation, the grains of the material will grow across the seam and form a monolithic block of material. In order for this process to be successful, the

parts have to be very flat and smooth i.e. shape and surface roughness very well defined, such that the material is in very good contact.

Although available for several decades as a joining technique for various materials and proven by e.g. CERN on a laboratory scale for accelerator parts, the process of diffusion-bonding is assessed to be not yet mature enough for the fabrication process of accelerator structures on an industrial scale. Especially the high processing temperature ($>1000\,^\circ$C) and pressure in combination with the highly accurate (micrometer tolerance) soft-copper parts poses significant risks i.e. failure of the bonding process will cause all parts to be rejects. Given the latest result in brazing X-band accelerator structures by PSI [25], it is advised from an industry point of view to design future accelerator structures to be joined by a brazing procedure. Figure 23 shows a Helium leak test of a brazed and bolted assembly.
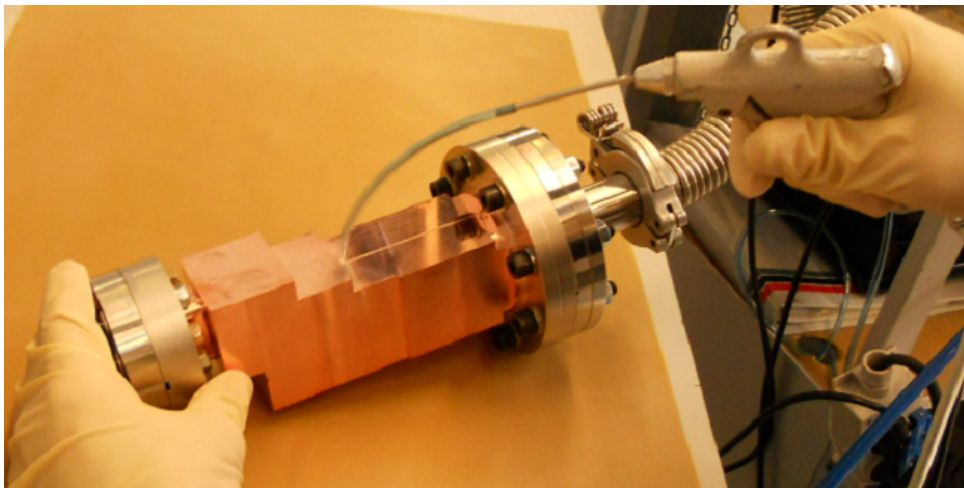


Figure 23: Helium leak testing of a brazed and bolted assembly.

After any joining technique, leak testing is performed as one of the last (mechanical) testing steps, often down to $10^{-10}$ mbar. During this test, the assembly is evacuated to a very low pressure by means of a pump and all the seams are sprayed with helium from the outside. If the detector attached to the pump detects helium, this is a sign that the structure is not vacuum tight.

### 4.4.5 Packaging

Given the fragile nature of the parts i.e. especially the center zone with the high RF power packaging is a crucial step in shipping the parts to the end customer. Packaging of individual discs is mostly done in membrane boxes (Fig. 24 left).

For (sub-)assemblies, more dedicated packaging (Fig. 24 right) has to be designed such that the products can be shipped with regular transport methods e.g. air/train/truck. Depending on the type of assembly it can be necessary to ship under certain conditions e.g. packed under dry nitrogen atmosphere, under vacuum, shock-proof.

Design and realization by Eindhoven University of Technology, The Netherlands
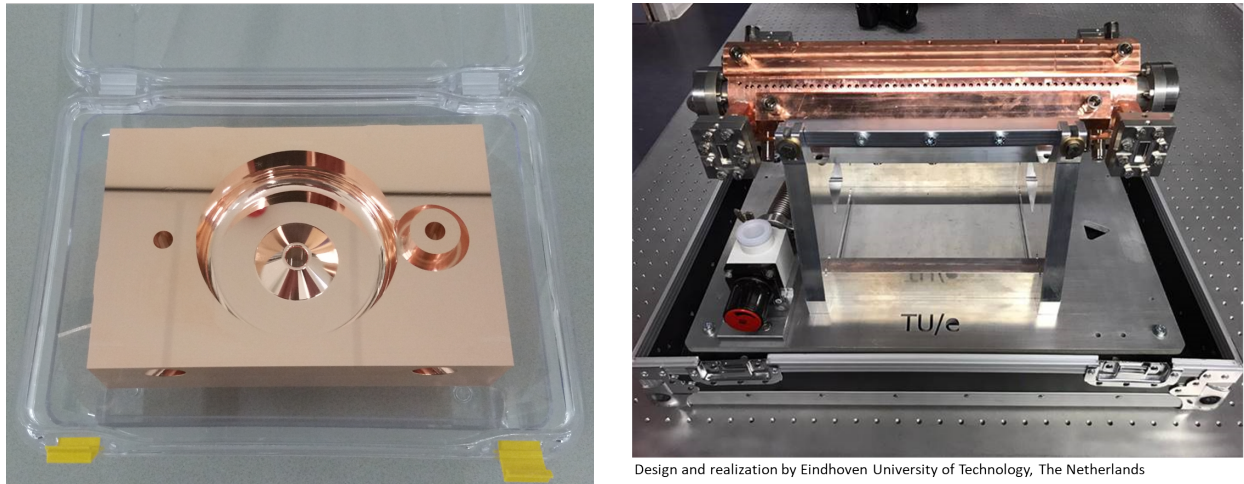
Figure 24:  Transport tools for mono-parts off-the-shelf available membrane boxed can be used (left) while for (sub)assemblies more dedicated tooling has to be developed (right).

## 4.5  Fabrication optimization

### 4.5.1  Symmetrical tolerances

In order to cope with variations in the manufacturing process, the aim in general is to machining a dimension to the value that is half-way in between the upper- and lower-tolerance. This leaves maximum room for variations in positive as well as negative direction. If the CAD-files do not include the tolerances in the form of full Product and Manufacturing Information (PMI), asymmetrical tolerances on drawing require a significant amount of manual input upon programming numerical controlled machines using the nominal 3D file of the product. This is not only labour intensive and hence costly, but also error-prone activity as the general format for dimension A ($A_x^y$) allows various asymmetrical tolerance bands as $x$ and $y$ can have various values with $x < y$. Some examples on a dimension of 80 mm and a tolerance bandwidth of 0.01 mm: $A_x^y$. Figure 25 shows examples of tolerance bands.
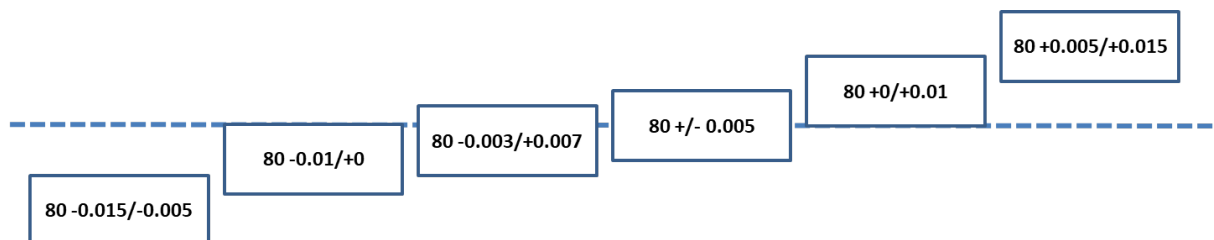


Figure 25:  Examples of tolerance bands with equal nominal dimension of 80 mm and equal bandwidth of 0.01 mm.

Hence it is highly advised to use symmetrical tolerances on drawing $A_{-x}^{+x}$. i.e. the dimension with asymmetrical tolerance of $80_0^{+0.01}$ mm becomes $80.005_{-0.005}^{+0.005}$ To facilitate the machinist in aiming for the dimension half-way between the edges of the tolerance bandwidth.

### 4.5.2 Standardized machine tooling

By standardization of the disc that form the accelerator stack, especially the outside diameter, various machine tools i.e. jigs to clamp the parts on the lathes, mills and cleaning station can be reused from previous x-band projects. In general it would be beneficial for serial-production if the accelerator community will continue further standardization of parts including mono-parts e.g. flanges, gaskets and (sub-) assemblies e.g. bi-directional couplers, pumping ports, splitters, loads.

## 4.6 Estimated cost breakdown

The material costs, i.e., price of the raw copper material, is not included in this section as this is highly depended on batch size and actual market price. The production costs of the mono-parts can be divided into several categories (Table 8) following the manufacturing flow. The items listed under General are Non-Recurring Engineering (NRE) cost that are related to programming the CNC-machines and hence only applicable for a new design, i.e., once a particular design has been manufactured, these costs are omitted in all following production runs.

As mentioned in section 4.5.2, the current design is such that the jigs, to hold the parts on the machines, can be reused from previous projects. Hence they are not taken into account on this cost breakdown.

As the tools (mill and lathe cutters) wear out over time, these have to be replaces at regular intervals in order to machine the parts with the given accuracy and surface roughness. Depending on the amount of wear, a fraction of their cost is included in the cost of the structure.

The machining steps are divided into two categories, pre- and end-machining, where the pre-machining steps take place in a regular machine shop with Precision-Technology (PT) and High-Precision-Technology (HPT) capabilities. End-machining will take place in a dedicated manufacturing area in which the Ultrahigh-Precision-Technology (UPT) machines are placed in a temperature controlled environment with a maximum temperature fluctuation of $\pm\,0.1\,^{\circ}$C

It is foreseen that the manufacturing strategy to date can be further optimized due to new developments in the HPT and UPT machining accuracy and combined milling/turning machine centers (Table 8 right two columns).

Table 8: Cost breakdown.

| Item | Operation | To date | | Optimized | |
|---|---|---|---|---|---|
| | | Costs | Total | Costs | Total |
| General | Work preparation | 1.5% | | 1.5% | |
| | Programming PT/HPT | 3.1% | 12.3% | 3.1% | 12.3% |
| | Programming UPT | 4.6% | | 4.6% | |
| | Programming 3D metrology | 3.1% | | 3.1% | |
| Tooling | Mill | 1.5% | 4.6% | 1.5% | 4.6% |
| | Diamond tool | 3.1% | | 3.1% | |
| Pre machining | Sawing | 1.5% | | 1.5% | |
| | Turning PT | 13.0% | 22.1% | 15.0% | 18.0% |
| | Milling HPT | 6.1% | | – | |
| | Annealing | 1.5% | | 1.5% | |
| End machining | Flycutting | 5.0% | | – | |
| | Turning UPT Pre-machining | – | | 15% | |
| | Turning UPT End-machining | 39.0% | 61.0% | 22.5% | 54.2% |
| | Cleaning | 1.7% | | 1.7% | |
| | Metrology | 15.3% | | 15.0% | |
| | | **100%** | | **90%** | |

# References

[1] M. Diomede,
*High-gradient structures and RF systems for high-brightness electron linacs*,
PhD thesis, Sapienza University of Rome, 2020,
URL: https://iris.uniroma1.it/retrieve/handle/11573/1357033/1347035/Tesi_dottorato_Diomede.pdf.

[2] *ANSYS Electronics Desktop website*,
URL: http://www.ansys.com/products/electronics/ansys-electronics-desktop.

[3] *MATLAB page on Wikipedia*,
URL: https://en.wikipedia.org/wiki/MATLAB.

[4] Z. D. Farkas et al., *SLED: A METHOD OF DOUBLING SLAC's ENERGY*,
Proceedings of the 9th International Conference on High-Energy Accelerators, 1976,
576, URL: https://inspirehep.net/literature/94052.

[5] LAPOSTOLLE ED PM, SEPTIER ED AL, *LINEAR ACCELERATORS*, North-Holland
Publ Co, Amsterdam, Neth, and Wiley Interscience Div, John Wiley & Sons, Inc (1970),
DOI: 10.1007/978-3-642-16483-5{\_}3364.

[6] R. B. Neal, *Design of Linear Electron Accelerators with Beam Loading*,
Journal of Applied Physics **29** (1958) 1019, ISSN: 0021-8979,
DOI: 10.1063/1.1723355,
URL: http://aip.scitation.org/doi/10.1063/1.1723355.

[7]   M. Diomede et al.,
      *Preliminary RF design of an X-band linac for the EuPRAXIA at SPARC_LAB project*,
      Nuclear Instruments and Methods in Physics Research, Section A: Accelerators,
      Spectrometers, Detectors and Associated Equipment (2018), ISSN: 01689002,
      DOI: 10.1016/j.nima.2018.01.032.

[8]   M. Diomede et al.,
      *RF Design of the X-band Linac for the EuPRAXIA at SPARC_LAB Project*,
      Proc. 9th International Particle Accelerator Conference (IPAC'18), Vancouver, BC,
      Canada, 29 April-04 May 2018, International Particle Accelerator Conference 9,
      JACoW Publishing, Geneva, Switzerland, 2018, 4422, ISBN: 978-3-95450-184-7,
      DOI: doi:10.18429/JACoW-IPAC2018-THPMK058,
      URL: http://jacow.org/ipac2018/papers/thpmk058.pdf.

[9]   A. Lunin, V. Yakovlev, A. Grudiev, *Analytical solutions for transient and steady state
      beam loading in arbitrary traveling wave accelerating structures*,
      Physical Review Special Topics - Accelerators and Beams **14** (2011) 52001,
      ISSN: 10984402, DOI: 10.1103/PhysRevSTAB.14.052001,
      URL: https://link.aps.org/doi/10.1103/PhysRevSTAB.14.052001.

[10]  P. Wang et al.,
      *The RF Design of a Compact, High Power Pulse Compressor with a Flat Output Pulse*,
      Proc. of International Particle Accelerator Conference (IPAC'16), Busan, Korea, May
      8-13, 2016, International Particle Accelerator Conference 7,
      JACoW, Geneva, Switzerland, 2016, 3591, ISBN: 978-3-95450-147-2,
      DOI: doi:10.18429/JACoW-IPAC2016-THPMW022,
      URL: http://jacow.org/ipac2016/papers/thpmw022.pdf.

[11]  P. Wang et al., *rf design of a pulse compressor with correction cavity chain for
      klystron-based compact linear collider*,
      Physical Review Accelerators and Beams **20** (2017) 112001, ISSN: 2469-9888,
      DOI: 10.1103/PhysRevAccelBeams.20.112001, URL: https:
      //link.aps.org/doi/10.1103/PhysRevAccelBeams.20.112001.

[12]  R. M. Jones et al.,
      *Wakefield damping in a pair of X-band accelerators for linear colliders*,
      Physical Review Special Topics - Accelerators and Beams **9** (2006), ISSN: 10984402,
      DOI: 10.1103/PhysRevSTAB.9.102001.

[13]  R. M. Jones, *Wakefield suppression in high gradient linacs for lepton linear colliders*,
      Physical Review Special Topics - Accelerators and Beams **12** (2009), ISSN: 1098-4402,
      DOI: 10.1103/physrevstab.12.104801.

[14]  M. Dehler, I. H. Wilson, W. Wuensch,
      *A tapered damped accelerating structure for CLIC*,
      Proc. of 19th International Linear Accelerator Conference, Chicago, 1998, 1987,
      URL: https://cds.cern.ch/record/364530.

[15]  C. Achard et al., *An Asset Test of the CLIC Accelerating Structure*,
      Proc. of the 7th European Particle Accelerator Conference, Vienna Austria, 2000,
      URL: https://cds.cern.ch/record/452944.

[16]  R. Jones et al.,
      *Dipole wakefield suppression in high phase advance detuned linear accelerators for the JLC/NLC designed to minimise electrical breakdown and cumulative BBU*,
      Proc. of the 2001 Particle Accelerator Conference, Chicago, 2001, 3810,
      DOI: 10.1109/PAC.2001.988261.

[17]  *GdfidL*, URL: www.gdfidl.de.

[18]  *CPI website*, URL: http://www.cpii.com/.

[19]  W. Wuensch et al., *Experience Operating an X-band High-Power Test Stand at CERN*,
      Proc. 5th International Particle Accelerator Conference (IPAC'14), Dresden, Germany,
      June 15-20, 2014, International Particle Accelerator Conference 5,
      JACoW, Geneva, Switzerland, 2014, 2288, ISBN: 978-3-95450-132-8,
      DOI: https://doi.org/10.18429/JACoW-IPAC2014-WEPME016,
      URL: http://jacow.org/ipac2014/papers/wepme016.pdf.

[20]  W. Wuensch, *High-Gradient RF Development and Applications*, Proc. of Linear
      Accelerator Conference (LINAC'16), East Lansing, MI, USA, 25-30 September 2016,
      Linear Accelerator Conference 28, JACoW, Geneva, Switzerland, 2017, 368,
      ISBN: 978-3-95450-169-4,
      DOI: https://doi.org/10.18429/JACoW-LINAC2016-TU2A04,
      URL: http://jacow.org/linac2016/papers/tu2a04.pdf.

[21]  *Canon website*, URL: https://etd.canon/en/product/category/microwave/klystron.html.

[22]  N. C. Lasheras et al.,
      *Commissioning of XBox-3: A Very High Capacity X-band Test Stand*, Proc. of Linear
      Accelerator Conference (LINAC'16), East Lansing, MI, USA, 25-30 September 2016,
      Linear Accelerator Conference 28, JACoW, Geneva, Switzerland, 2017, 568,
      ISBN: 978-3-95450-169-4,
      DOI: https://doi.org/10.18429/JACoW-LINAC2016-TUPLR047,
      URL: http://jacow.org/linac2016/papers/tuplr047.pdf.

[23]  A. Grudiev, S. Calatroni, W. Wuensch,
      *New local field quantity describing the high gradient limit of accelerating structures*,
      Physical Review Special Topics - Accelerators and Beams (2009),
      DOI: 10.1103/physrevstab.12.102001.

[24]  K. Papke, C. Rossi, G. C. Burt, *Coupled RF-Thermo-Structural Analysis of CLIC
      Traveling Wave Accelerating Structures*,
      tech. rep. CERN-ACC-2020-0019. CLIC-Note-1158, Geneva: CERN, 2020,
      URL: http://cds.cern.ch/record/2730555.

[25]  P. Craievich et al.,
      *Consolidation and Extension of the High-gradient LINAC RF Technology at PSI*,
      Proc. 29th Linear Accelerator Conference (LINAC'18), Beijing, China, 16-21 September
      2018, Linear Accelerator Conference 29,
      JACoW Publishing, Geneva, Switzerland, 2019, 937, ISBN: 978-3-95450-194-6,
      DOI: doi:10.18429/JACoW-LINAC2018-THPO115,
      URL: http://jacow.org/linac2018/papers/thpo115.pdf.